

Electronic Supplementary Information

Enhanced electrocatalytic activity via phase transitions in strongly correlated SrRuO₃ thin films

Sang A Lee,^{a,b*} Seokjae Oh,^{a*} Jae-Yeol Hwang,^c Minseok Choi,^{d,e} Chulmin Youn,^f Ji Woong Kim,^g Seo Hoyung Chang,^h Sungmin Woo,^a Jong-Seong Bae,ⁱ Sungkyun Park,^g Young-Min Kim,^{c,j} Suyoun Lee,^k Taekjib Choi,^f Sung Wng Kim,^j and Woo Seok Choi^a

^a Department of Physics, Sungkyunkwan University, Suwon 16419, Korea

^b Institute of Basic Science, Sungkyunkwan University, Suwon 16419, Korea

^c Center for Integrated Nanostructure Physics, Institute for Basic Science (IBS) Sungkyunkwan University, Suwon 16419, Korea

^d Materials Modeling and Characterization Department, Korea Institute of Materials Science, Changwon 51508, Korea

^e Department of Physics, Inha University, Incheon 22212, Korea

^f Hybrid Materials Research Center, Department of Nanotechnology and Advanced Materials Engineering, Sejong University, Seoul 05006, Korea

^g Hybrid Materials Research Center, Department of Nanotechnology and Advanced Materials Engineering, Sejong University, Seoul 05006, Korea

^h Department of Physics, Chung-Ang University, Seoul 06974, Korea

ⁱ Busan Center, Korea Basic Science Institute, Busan 46742, Korea

^j Department of Energy Sciences, Sungkyunkwan University, Suwon 16419, Korea

^k Electronic Materials Research Center, Korea Institute of Science and Technology, Seoul 02792, Korea

Experimental detail

Thin film growth and structural characterization

High-quality epitaxial SrRuO₃ thin films were grown on TiO₂-terminated SrTiO₃ (for optical experiments) and 0.5 wt% Nb-doped SrTiO₃ (for Oxygen evolution reaction (OER) analyses) substrates using pulsed laser epitaxy (PLE). A KrF excimer laser ($\lambda = 248$ nm; Lightmachinery, IPEX 864) with a fluence of ~ 1.5 J cm⁻² and repetition rate of 2 Hz was used for the ablation of a sintered target. The substrate temperature was fixed at 700 °C with varying $P(\text{O}_2)$ ranging from 3×10^{-1} to 1×10^{-4} Torr.^{1,2} The vertical distance between the target and the substrate was fixed to 65 mm. Crystalline structures of the thin films were determined using high-resolution X-ray diffraction (XRD, Rigaku SmartLab). The thicknesses of films were fixed at ~ 30 nm, as measured by X-ray reflectometry (XRR) (Fig. S1(a)). Figs. S1(b) and S2 show XRD θ - 2θ scans and rocking curves of the thin films grown at different $P(\text{O}_2)$. The results indicate well-oriented single-crystalline thin films without any secondary phases and good crystalline quality (FWHM $\leq 0.02^\circ$). An atomic force microscope (AFM, Park Systems NX10) with a Si probe tip (Budget sensors ContAl-G) was used to confirm the surface topography (inset of Fig. S2). Root-mean-square (RMS) roughnesses of 0.687 and 0.821 nm were obtained for the SrRuO₃ thin films grown above ($P(\text{O}_2) = 3 \times 10^{-2}$ Torr) and below ($P(\text{O}_2) = 1 \times 10^{-2}$ Torr) $P_c(\text{O}_2)$, respectively, indicating atomically flat surfaces with preserved step-and-terrace atomic structures of the substrate for both samples. Fig. S3 shows {204} SrTiO₃ Bragg reflections with φ angles of 0, 90, 180, and 270°. The parameter of the SrRuO₃ orthorhombic unit cell parameter of $a \neq b \neq c$ and $\alpha \approx \beta \approx \gamma \approx 90^\circ$ with additional distortion can be calculated to the pseudocubic unit cell ($a_{\text{pc}} = a_{\text{STO}}$, $b_{\text{pc}} = a_{\text{STO}}$, c_{pc}) through the following relationships,^{3,4}

$$a_{\text{pc}} = \frac{c_0}{2},$$

$$b_{pc} = \frac{\sqrt{a_o^2 + b_o^2 + 2a_o^2 b_o^2 \cos \gamma_o}}{2},$$

$$c_{pc} = \sqrt{\frac{a_o^2 + b_o^2 - 2b_{pc}^2}{2}}.$$

Table S1 shows the calculated lattice parameters of SrRuO₃ thin films on SrTiO₃ substrates grown at various $P(O_2)$.

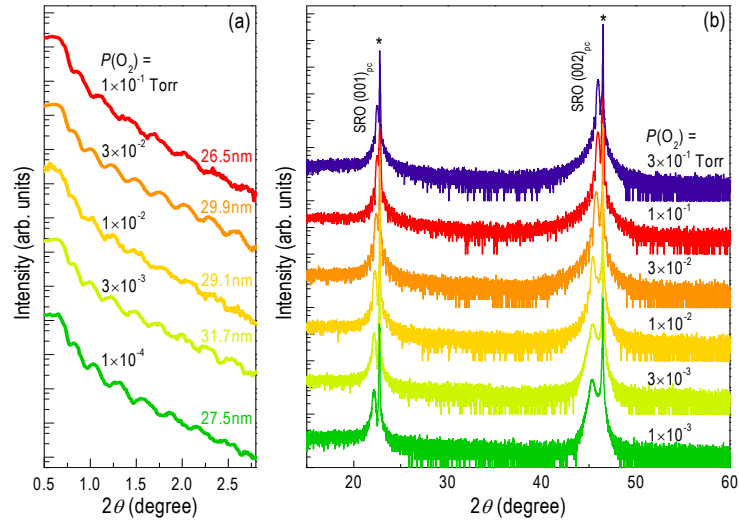


Fig. S1. XRR and XRD θ - 2θ scans for SrRuO₃ thin films on SrTiO₃ substrates grown at different $P(O_2)$. (a) XRR results show that SrRuO₃ thin films have thickness of ~ 30 nm. (b) XRD results indicate single-crystalline SrRuO₃ thin films are grown over a wide range of $P(O_2)$ without any secondary phases.

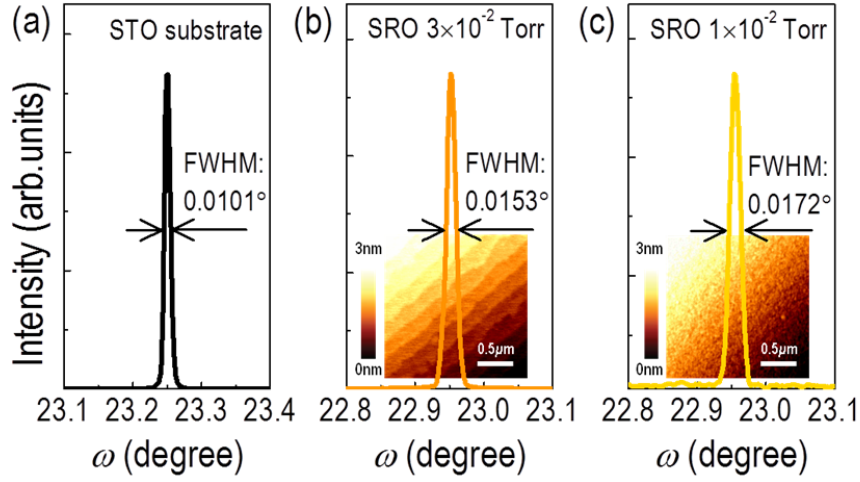


Fig. S2. Rocking curve scans and atomic force microscopy images of epitaxial SrRuO₃ thin films. Rocking curve scans of (a) SrTiO₃ substrate, SrRuO₃ thin film with (b) orthorhombic and (c) tetragonal structures. Both the AFM images in the insets show the step-and-terrace structure.

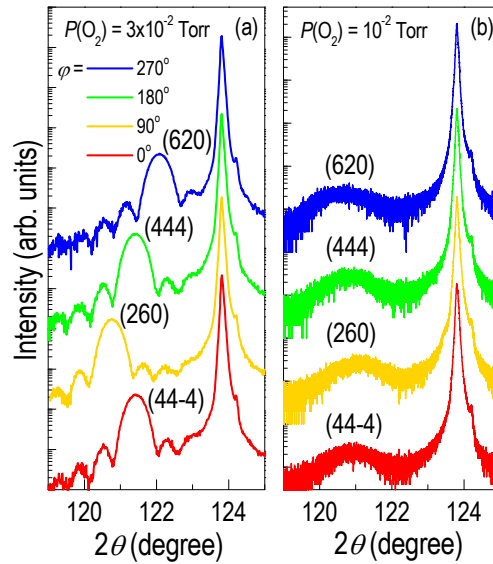


Fig. S3. Off-axis X-ray diffraction for the orthorhombic and tetragonal SrRuO₃ thin films. $(20L)_{pc}$ XRD reflections of SrRuO₃ thin films grown at $P(O_2) =$ (a) 3×10^{-2} and (b) 1×10^{-2} Torr, around the SrTiO₃ (204) Bragg reflections with configuration of $\varphi = 0, 90, 180,$ and 270° .

	a (Å)	b (Å)	c (Å)	γ (°)	orthorhombic distortion (a/b)
Bulk ⁵	5.567	5.530	7.845	90	1.00669
3×10^{-1} Torr	5.592	5.548	7.810	89.020	1.00794
1×10^{-1} Torr	5.596	5.549	7.810	88.976	1.00847
3×10^{-2} Torr	5.608	5.564	7.810	88.709	1.00791
1×10^{-2} Torr	5.523	5.523	7.983	90	1
1×10^{-3} Torr	5.523	5.523	7.986	90	1

Table S1. Lattice parameters of SrRuO₃ thin films grown at various $P(\text{O}_2)$.

X-ray photoemission spectroscopy

The chemical structure was studied at room temperature using XPS (Theta Probe, Thermo) with a monochromated Al-K α X-ray source ($h\nu = 1486.6$ eV). The step size was 0.1 eV at a pass energy of 50.0 eV with a 400 μm spot size. All the peak positions were calibrated using the C 1s photoemission signal (284.5 eV). In order to analyze the spectra in detail, we deconvoluted the peaks using a mixed Gaussian-Lorentzian function.⁶

Ellipsometry

The optical properties of the SrRuO₃ thin films were investigated using spectroscopic ellipsometers (VASE and M-2000, J. A. Woollam Co.) at room temperature. The optical spectra were obtained between 0.74 and 5.5 eV for incident angles of 70 and 75°. A two-layer model (SrRuO₃ thin film on SrTiO₃ substrate) was sufficient for obtaining physically reasonable spectroscopic dielectric functions of SrRuO₃ that reproduced the literature spectrum.

Theoretical calculation

The calculations were performed using the projector augmented-wave method⁷ and the generalized gradient approximation exchange-correlation functional⁸ with a Hubbard- U correction, as implemented in the Vienna ab initio simulation package.⁹ The electronic wave functions were described using a planewave basis set with an energy cutoff of 400 eV. A rotationally invariant $+U$ method¹⁰ was applied to the Ru $4d$ ($U_{\text{eff}} = 2.1$ eV) orbitals, the value for which was used in previous literature.^{11,12} The calculations for vacancy defects in SrRuO₃ were performed using 160-atom supercells. The wavefunctions were expanded in a plane-wave basis set with an energy cutoff of 400 eV, and integrations over the Brillouin zone were carried out using the $4 \times 4 \times 2$ k -point mesh. The atomic coordinates were relaxed until the force acting on each atom was reduced to less than 0.05 eV \AA^{-1} . The formation energy of each vacancy was evaluated by the equation in a reference,¹³ by considering the secondary phases of SrO and RuO₂. As an estimate for the sample growth, we set the oxygen chemical potentials (μ_{O}) to -1.39 and -1.58 eV, corresponding to $P(\text{O}_2)$ values of 10^{-1} and 10^{-3} Torr, respectively at a temperature of $700 \text{ }^\circ\text{C}$.

Theoretical calculation of the vacancy formation energy supports the elemental vacancy engineering of the crystal structure. As shown in Table S2, vacancies are likely to form in the tetragonal SrRuO₃, and the RuO vacancy may predominantly prevail due to it having the lowest formation energy, which is consistent with the spectroscopic observations. For an orthorhombic structure, the formation of the vacancies would be relatively suppressed since the formation energy is much higher compared to that of tetragonal SrRuO₃.

Vacancy type	Tetragonal structure (eV)	Orthorhombic structure (eV)
Ru	0.30	0.54
O	-0.19	1.55
RuO	-0.36	1.09

Table S2. Formation energy of different types of vacancies in SrRuO₃ thin films with distinctive crystal structures. Theoretical calculation of formation energy (in eV) suggests that O and RuO vacancies spontaneously form in the tetragonal SrRuO₃ thin films, while the formation energy in the orthorhombic structure is positive for all the types of defects studied.

In order to estimate the contribution of defects compared to that of the structural phase transition, we calculated the density of states (DOS) of stoichiometric orthorhombic SrRuO₃ (Fig. S4(a)), stoichiometric tetragonal SrRuO₃ (Fig. S4(b)), and RuO defect-induced tetragonal Sr₃₂Ru₃₁O₉₅ (Fig. S4(c)). The main modifications in the electronic structure indicated by optical spectroscopy are represented by red and green arrows: The occupied O 2*p* level decreases (red) and the unoccupied Ru 4*d* *e_g* level increases (green) when the crystal structure changes from orthorhombic to tetragonal. Interestingly, the DOS of the stoichiometric (Fig. S4(b)) and the RuO deficient (Fig. S4(c)) tetragonal SrRuO₃ have the same features in terms of the main electronic structure, indicating that the structural phase transition is a crucial factor for the electronic structure modification in the SrRuO₃ grown at low *P*(O₂). In other words, elemental vacancies do not sufficiently contribute to changes in the electronic structure.

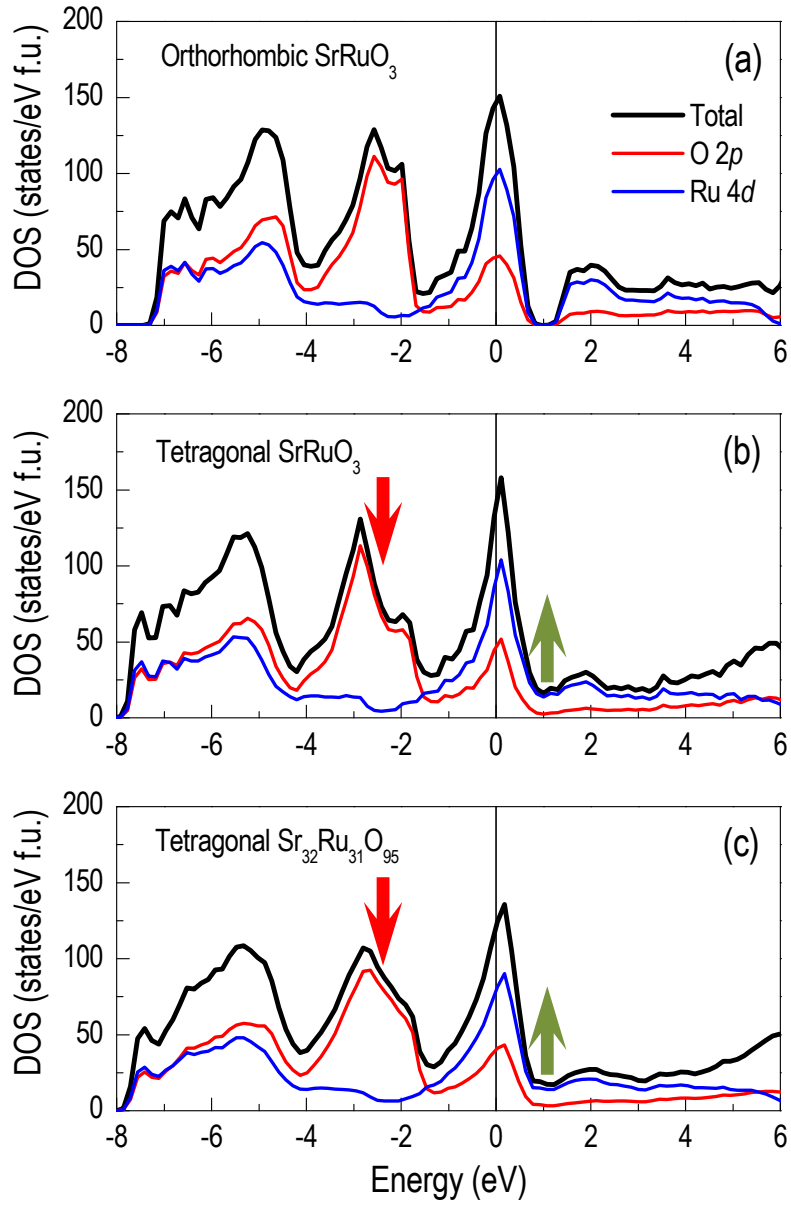


Fig. S4. Theoretical calculations of the density of states for the SrRuO_3 thin films. (a) Orthorhombic stoichiometric SrRuO_3 , (b) tetragonal stoichiometric SrRuO_3 , and (c) tetragonal RuO deficient $\text{Sr}_{32}\text{Ru}_{31}\text{O}_{95}$ thin films are shown for comparison.

Resistivity measurements

Resistivity as a function of temperature, $\rho(T)$, was measured using a low-temperature closed-cycle refrigerator (ARS-4HW, Advance Research Systems). The measurements were performed from 300 to 20 K, using the Van der Pauw method with In electrodes and Au wires.

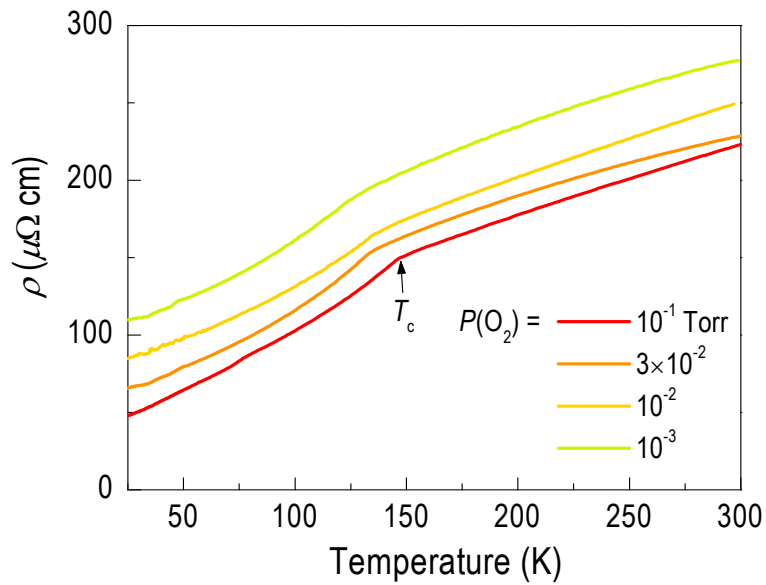


Fig. S5. Changes in the electronic properties of SrRuO₃ thin films. Resistivity as a function of temperature ($\rho(T)$) is shown for the SrRuO₃ thin films deposited at various $P(\text{O}_2)$. With decreasing $P(\text{O}_2)$, overall $\rho(T)$ increases which could be attributed to vacancy scattering.

Electrochemical measurements

A Vertex potentiostat (Ivium Technologies) was used for electrochemical measurements using the three-electrode method. Ag/AgCl (reference electrode), Pt mesh (counter electrode), and high-quality epitaxial SrRuO₃ thin films (working electrode) were used as the electrodes. The SrRuO₃ films were contacted with copper wires using silver epoxy (TED PELLA, INC.) and there was no noticeable contact resistance between samples and wires. The sample, except for the SrRuO₃ film surface, was sealed by coating PMMA, to avoid direct exposure of the conducting substrate to the electrolyte. We carefully soaked the SrRuO₃ thin films into the electrolyte below the contact region and the area of the working electrode was $4.5 \times 4.5 \text{ mm}^2$. The schematic diagram of the sample for electrochemical measurements is shown in Fig. S6. For the electrolyte, we used 1 M KOH prepared with deionized water, and the same amount of the surface areas of each sample was carefully soaked into the KOH solution, without submerging the contact region. The sweep rate for cyclic voltammetry was $5\text{-}50 \text{ mV s}^{-1}$. The trends of the OER activity between the orthorhombic and tetragonal SrRuO₃ thin films were the same, independent of the sweep rate. Note that the potential is shown vs. a reversible hydrogen electrode (RHE).

In order to confirm that the large increase in the current level in cyclic voltammetry originates indeed from OER, we performed several additional experiments. First, as shown in Fig. S7, we confirmed that the Nb:SrTiO₃ substrates do not affect the OER activity of SrRuO₃ thin films. Second, we measured several cyclic voltammetry curves at different potential sweep range to confirm the stability. Fig. S8 shows the reversible current-potential curves in SrRuO₃ thin films at lower potential range (initial stability test). These measurements have been conducted on all of our SrRuO₃ thin films to confirm the sample are stable at low potential ($\leq 1.3 \text{ V}$), which is well above the onset potential of OER ($\sim 1.25 \text{ V}$). The data of Fig. 5 in the main text have been taken

after these measurements. Based on this result, we believe that the low onset potential in tetragonal SrRuO₃ is due to the electrocatalytic reaction, and not coming from the materials oxidation. Third, Fig. S9(a) again shows reversible cyclic voltammetry sweep at low potential (≤ 1.3 V). These samples have been further tested using XRD to confirm that there is no change in the thickness or crystal structure of the thin films after several cycles of the electrochemical experiments. X-ray photoemission spectroscopy (XPS) shown in Fig. S10 also suggests that our samples are stable at low potential (≤ 1.3 V). We further performed the inductively coupled plasma-mass spectroscopy (ICP-MS) and we did not observe any noticeable Sr and Ru dissolution in KOH solution after the stability test up to 1.3 V for several cycles (Fig. S11). Indeed, we observed only small amount (~ 2 ppb) of Sr in the solution which was comparable to the reference solution and did not observe any Ru in the test solution (up to 1.3 V), for both orthorhombic and tetragonal SrRuO₃ thin films. We also show the solution after applying potential up to 1.7 V for comparison, where the elements (both Sr and Ru) are actually dissolved into the solution. Fig. S12 shows the chronoamperometric measurements as compared with cyclic voltammetry. While the SrRuO₃ thin film is known to dissolve in alkaline solution at a large applied voltage (> 1.5 V), current density well above the onset potential (up to ~ 1.4 V) is maintained, indicating consistent OER behavior.

Fig. S13 shows the Tafel plots for all the SrRuO₃ thin films with slope values of (i) 1×10^{-1} Torr: 77.7 mV dec^{-1} , (ii) 3×10^{-2} Torr: 66.2 mV dec^{-1} , (iii) 1×10^{-2} Torr: $107.4 \text{ mV dec}^{-1}$, (iv) 3×10^{-3} Torr: $108.5 \text{ mV dec}^{-1}$, and (v) 1×10^{-4} Torr: $106.1 \text{ mV dec}^{-1}$, respectively. Again, a clear distinction is demonstrated, indicating the difference in the kinetics of the OER between the SrRuO₃ thin films with different crystalline structures (orthorhombic and tetragonal).

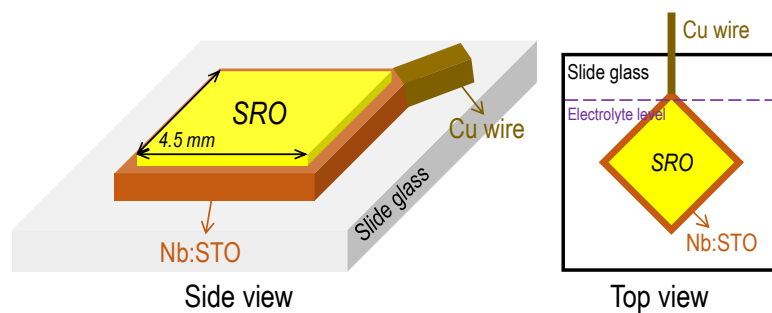


Fig. S6. Schematic diagram of SrRuO₃ thin film sample for the electrochemical measurements.

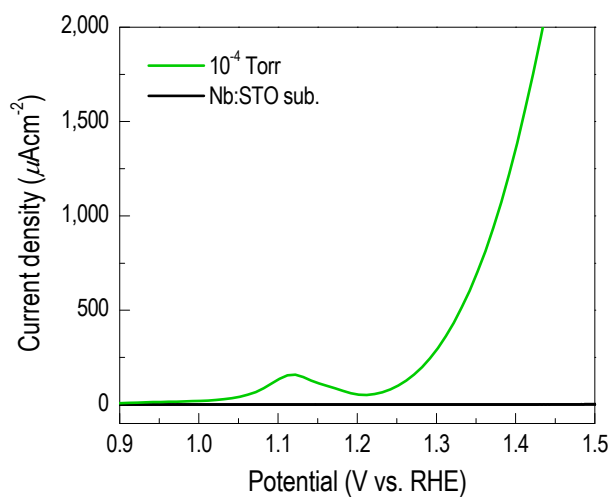


Fig. S7. Current-potential curves of SrRuO₃ thin film and Nb:SrTiO₃ substrate. Nb:SrTiO₃ substrate does not show any current in the whole potential range, which allows us to eliminate the contribution of the substrate to the observed OER activity in the SrRuO₃ thin films.

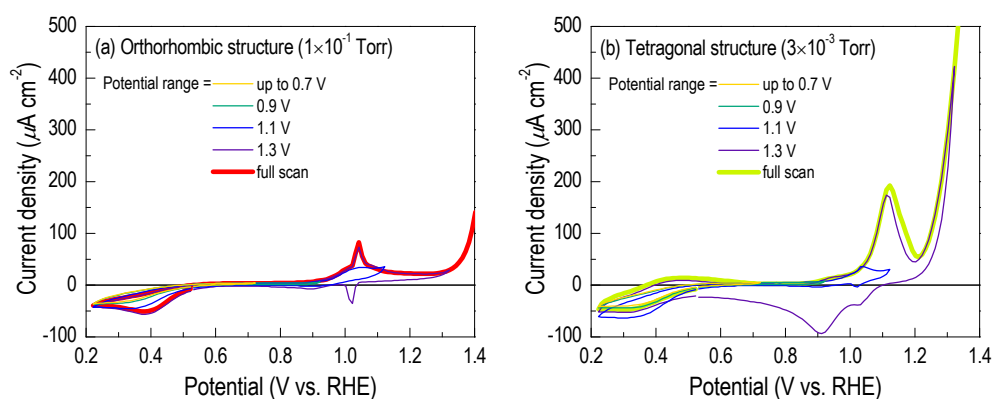


Fig. S8. The current-potential cycle in (a) orthorhombic and (b) tetragonal epitaxial SrRuO₃ thin films at lower potential range (initial stabilization test). The Figure shows the data with a scan rate of 50 mV s⁻¹, but the same systematic trend is observed for the same measurements with lower scan rates (5-50 mV s⁻¹).

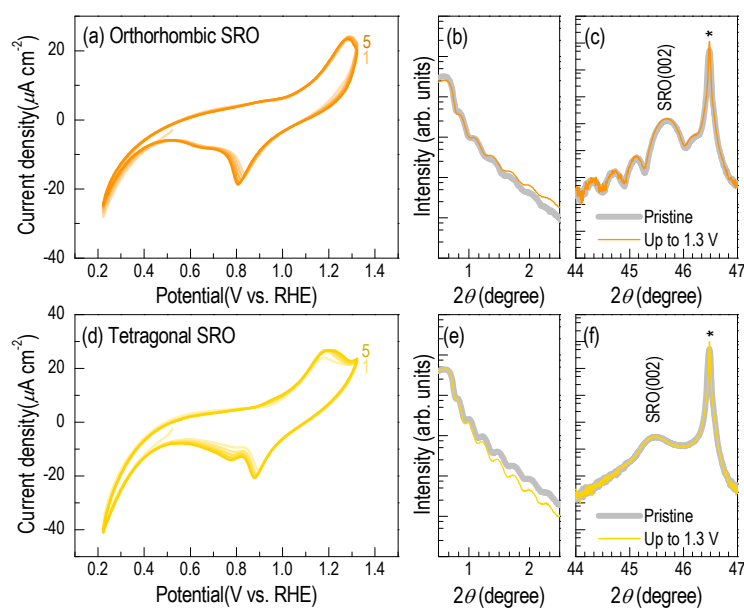


Fig. S9. Reversible cyclic voltammetry results at low potential range (< 1.3 V) of (a) orthorhombic and (d) tetragonal SrRuO₃ thin films. (b,c,e,f) XRD result for the SrRuO₃ sample before and after the initial stability test. Gray lines indicate pristine SrRuO₃ thin film and color lines indicate the same sample after the initial stability test, respectively.

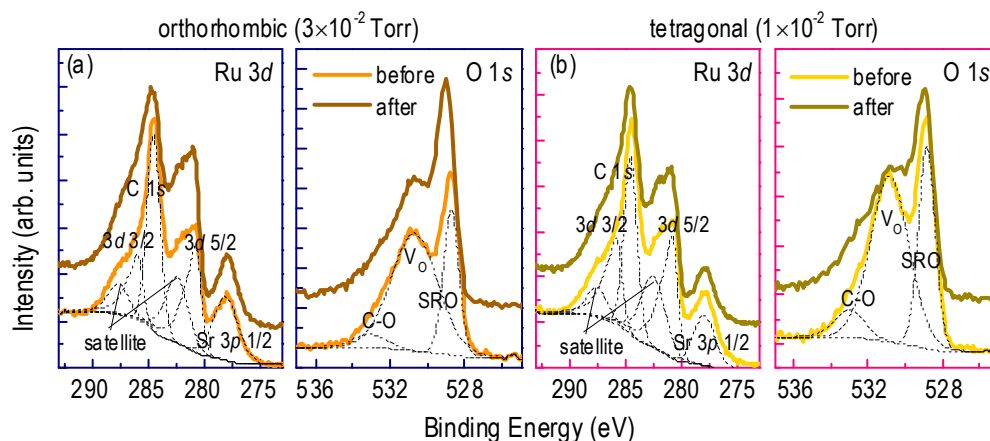


Fig. S10. X-ray photoemission spectroscopy for (a) orthorhombic and (d) tetragonal SrRuO₃ thin films before and after the initial stability test, respectively.

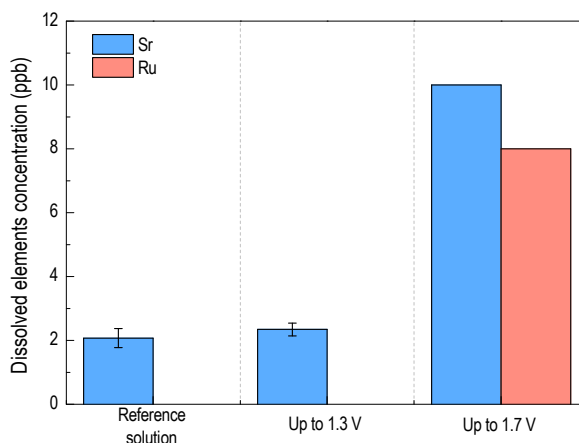


Fig. S11. Contents of dissolved elements in the KOH solution obtained by ICP-MS. Our results show negligible amount of dissolution of the sample both orthorhombic and tetragonal structure when the potential is applied up to 1.3 V, which is clearly higher than the onset potential of OER.

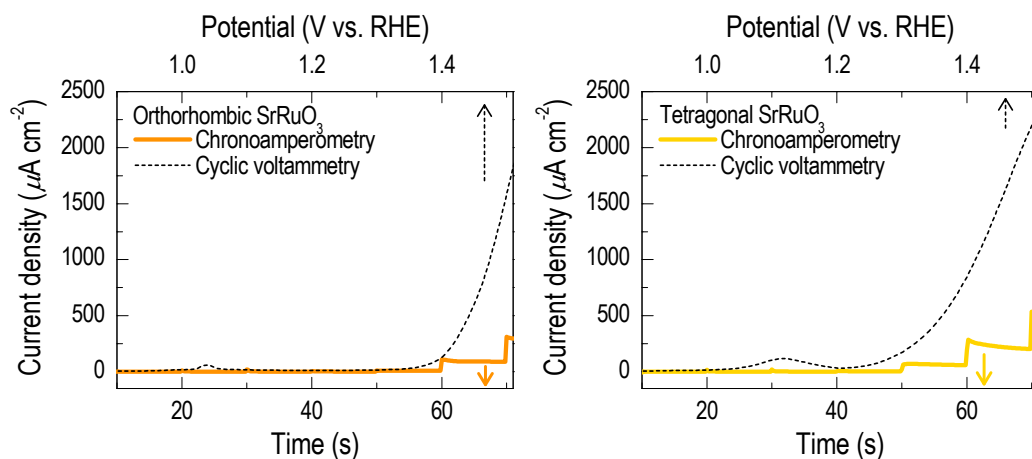


Figure S12. Chronoamperometric measurements on the orthorhombic and tetragonal SrRuO₃ epitaxial thin films grown at 3×10^{-2} and 1×10^{-2} Torr, respectively, in dark.

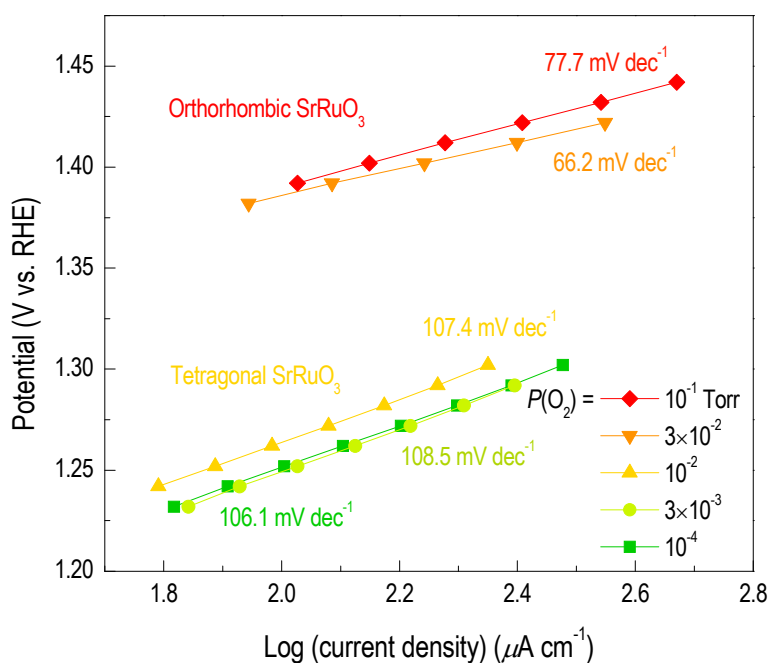


Fig. S13. Tafel plots of epitaxial SrRuO₃ thin films grown at different $P(O_2)$. Tafel plots show the tetragonal SrRuO₃ films have smaller overpotential than orthorhombic SrRuO₃ films.

References

1. S. Woo, H. Jeong, S. A. Lee, H. Seo, M. Lacotte, A. David, H. Y. Kim, W. Prellier, Y. Kim and W. S. Choi, *Sci. Rep.*, 2015, **5**, 7.
2. S. A. Lee, H. Jeong, S. Woo, J.-Y. Hwang, S.-Y. Choi, S.-D. Kim, M. Choi, S. Roh, H. Yu, J. Hwang, S. W. Kim and W. S. Choi, *Sci. Rep.*, 2016, **6**, 23649.
3. A. T. Zayak, X. Huang, J. B. Neaton and K. M. Rabe, *Phys. Rev. B*, 2006, **74**, 094104.
4. A. Vailionis, H. Boschker, W. Siemons, E. P. Houwman, D. H. A. Blank, G. Rijnders and G. Koster, *Phys. Rev. B*, 2011, **83**, 064101.
5. C. W. Jones, P. D. Battle, P. Lightfoot and W. T. A. Harrison, *Acta Crystallogr., Sect. C*, 1989, **45**, 365-367.
6. R. K. Sahu, S. K. Pandey and L. C. Pathak, *J. Solid. State. Chem.*, 2011, **184**, 523-530.
7. P. E. Blöchl, *Phys. Rev. B*, 1994, **50**, 17953-17979.
8. J. P. Perdew, K. Burke and M. Ernzerhof, *Phys. Rev. Lett.*, 1996, **77**, 3865-3868.
9. G. Kresse and J. Hafner, *Phys. Rev. B*, 1993, **48**, 13115-13118.
10. S. L. Dudarev, G. A. Botton, S. Y. Savrasov, C. J. Humphreys and A. P. Sutton, *Phys. Rev. B*, 1998, **57**, 1505-1509.
11. P. Mahadevan, F. Aryasetiawan, A. Janotti and T. Sasaki, *Phys. Rev. B*, 2009, **80**, 035106.
12. K. Gupta, B. Mandal and P. Mahadevan, *Phys. Rev. B*, 2014, **90**, 125109.
13. M. Choi, A. Janotti and C. G. Van de Walle, *Phys. Rev. B*, 2013, **88**, 214117.